





Mode switching dynamics in organic polariton lasing

Antti J. Moilanen ^{1,2,*} Kristín B. Arnardóttir ^{3,4,5} Jonathan Keeling ⁵ and Päivi Törmä ^{1,†}


¹*Department of Applied Physics, Aalto University School of Science, FI-00076 Aalto, Finland*

²*Photonics Laboratory, ETH Zürich, CH-8093 Zürich, Switzerland*

³*DTU Fotonik, Technical University of Denmark, 2800 Kongens Lyngby, Denmark*

⁴*NanoPhoton-Center for Nanophotonics, Technical University of Denmark, 2800 Kongens Lyngby, Denmark*

⁵*SUPA, School of Physics and Astronomy, University of St Andrews, KY16 9SS St Andrews, United Kingdom*

 (Received 16 June 2022; revised 21 October 2022; accepted 25 October 2022; published 3 November 2022)

We study the dynamics of multimode polariton lasing in organic microcavities by using a second-order cumulant equation approach. By inspecting the time evolution of the photon mode occupations, we show that if multiple lasing peaks are observed in time-integrated mode occupations, the reason can be either bimodal lasing or temporal switching between several modes. The former takes place within a narrow range of parameters while the latter occurs more widely. We find that the origin of the temporal switching is different in the weak- and strong-coupling regimes. At weak coupling the different gradients of mode occupation vs pump power is the determining factor, while for strong coupling it is changes in the eigenmodes and gain spectrum upon pumping. This difference is revealed by investigating the photoluminescence and momentum-resolved gain spectra. Our results underscore the importance of understanding the time evolution of the populations when characterizing the lasing behavior of a multimode polariton system, and show how these features differ between weak and strong coupling.

DOI: [10.1103/PhysRevB.106.195403](https://doi.org/10.1103/PhysRevB.106.195403)

I. INTRODUCTION

In a system where lasing occurs, switching between lasing modes can occur, as a function of parameters (e.g., excitation power) or as a function of time. Mode switching is known to occur in semiconductor lasers that support several densely spaced longitudinal modes. Multiple lasing peaks in the time-integrated luminescence spectrum, as well as temporal switching between the modes, have been observed in many different contexts [1–5]. The origin and nature of such mode switching differs between systems. For example, the mode switching in edge-emitting semiconductor lasers and vertical cavity surface emitting lasers (VCSELs) has been attributed to spatial hole burning [6–9] and to four-wave mixing [10]. Understanding the nature of mode switching in a given system, and how to control it, is an important step toward enabling applications.

Exciton-polaritons, polaritons for brevity, are the hybrid of a photon and an exciton under strong light-matter coupling. Strong coupling can be engineered by creating optical microcavities filled with an active layer of emitter material. The active layer can take several forms, including inorganic semiconductors, two-dimensional materials such as transition metal dichalcogenides, or, the focus of this paper, organic molecules. Polariton lasing (or polariton condensation) has been studied extensively during the past two decades [11–13].

While the majority of the experimental and theoretical works have focused on single-mode polariton lasing, multimode operation has been reported as well. Switching of

macroscopic polariton population between different spatial modes or momentum states has been observed as a function of pump power [14–18]. The switching between higher- and lower-energy polariton modes has been attributed to polariton-polariton scattering, which is stimulated by Bose enhancement at higher pump powers, driving the relaxation of polaritons to the lowest-energy mode [17–20]. Typically, mode switching has been observed only for specific detuning conditions. In coupled wells or lattices of coupled polariton condensates, competition between different modes has been studied experimentally [21–26] and numerically by using the generalized Gross-Pitaevskii equations [27,28]. Recently, it was noted that simultaneous polariton lasing can occur in a vertical lasing mode and a horizontal guided mode in planar microcavities, and that such phenomena could have taken place in several previous experiments where polariton lasing in the vertical lasing mode has been reported with ZnO-based microcavities [29]. Mode competition dynamics has also recently been explored in InGaAs-based cavities [30]. In closely related experiments on photon Bose-Einstein condensates (BECs), with weak light-matter coupling in dye-filled microcavities, multimode condensation has been observed experimentally and studied by second-order cumulant equations [31–34]. Similarly, for strongly coupled plasmonic BECs, multiple peaks near the ground state have been observed [35].

In our previous work [36], we introduced a model for multimode polariton lasing in organic microcavities and computed steady-state lasing phase diagrams as a function of pump strength and detuning of the photon modes from the exciton. We showed that at certain pump strengths multiple lasing peaks may be observed in the steady-state photon mode occupations. Our second-order cumulant model goes beyond mean-field descriptions, capturing the effects of nonlasing

*amoilanen@ethz.ch

†paivi.torma@aalto.fi

modes and fluctuations on the system's behavior. Retaining such fluctuations is important when considering switching: the (initially small) populations of nonlasing modes act as the seed for these modes to become macroscopically populated at later times. In contrast, for mean-field approaches, explicit seed or noise terms would be required.

In this paper, we investigate the dynamics of mode switching in multimode polariton lasing, and analyze the gain spectrum in more depth than in [36], including momentum-resolved gain spectra. While the model we consider is specific to organic molecules, the concepts we discuss have relevance more widely. We find that in the case where several lasing peaks are observed in the time-integrated mode occupations, the modes are not necessarily lasing *simultaneously*, but the lasing mode may switch (deterministically) as a function of time. Furthermore, even when only a single lasing peak is observed, switching between different modes can occur before the system reaches a steady state. We study mode switching in both weak- and strong-coupling regimes.

Mode switching occurs in general because the mode which lases first does not fully cross saturate the gain for other modes. This raises a question of what determines which other modes become competitive, and ultimately take over. At weak coupling, the choice of which mode is selected can be explained by a standard argument [37] considering the different thresholds and gradients of photon population vs pump of each mode: When several modes are above the threshold, the mode with highest gain will eventually suppress the others. At strong coupling, the situation becomes more complicated because of energy shifts. The polariton energies show a blueshift as a function of pump strength, due to effective interactions that arise from saturation of the gain medium. Importantly, we also show that the peak gain shifts towards higher energies as the pump strength increases. This shift can be attributed to dynamics of the vibrational degrees of freedom of the molecules. The mode switching at strong coupling occurs as a result of competition between both shifts in the gain and the polariton energies. Our model considers spatially homogeneous systems, thus our results suggest that mode switching does not necessarily require redistribution of real-space intensity.

The rest of the paper is organized as follows. In Sec. II, we present the system and the model. In Sec. III, we study the temporal characteristics of multimode lasing. In Sec. IV, we present the gain and photoluminescence spectra as a function of pump strength. In Sec. V we consider pulsed excitation, which is relevant for typical experiments on organic exciton-polariton systems. Finally, in Sec. VI we discuss the interpretation and implications of the results. The Appendixes provide technical details on the cumulant equations and results for time-integrated populations.

II. SYSTEM AND MODEL

A. Density matrix equation of motion

We consider a planar microcavity that hosts multiple photon modes and an active layer of emitters. We model the emitters as N_m vibrationally dressed two-level systems placed homogeneously in the cavity plane. The system is thus described by the Tavis-Cummings-Holstein Hamiltonian in the

rotating-wave approximation (RWA) [36,38,39]:

$$H = \sum_{\mathbf{k}} \omega_{\mathbf{k}} a_{\mathbf{k}}^\dagger a_{\mathbf{k}} + \sum_{n,\mathbf{k}} (g_{n,\mathbf{k}} a_{\mathbf{k}} \sigma_n^+ + g_{n,\mathbf{k}}^* a_{\mathbf{k}}^\dagger \sigma_n^-) + \sum_n \left[\frac{\varepsilon}{2} \sigma_n^z + \omega_v (b_n^\dagger b_n + \sqrt{S} (b_n^\dagger + b_n) \sigma_n^z) \right]. \quad (1)$$

Here ε is the transition energy of the molecule and Pauli matrices $\sigma_n^{z,+,-}$ correspond to the electronic states of molecule n . The operator b_n^\dagger creates a vibrational excitation of energy ω_v on molecule n while $a_{\mathbf{k}}^\dagger$ creates a photon with energy $\omega_{\mathbf{k}}$ in the cavity mode with wave vector \mathbf{k} .

The photon energies are given by $\omega_{\mathbf{k}} = \omega_0 + E_\rho(K_x^2 + K_y^2)/N_m$, where $K_{x,y}$ are integers labeling a discrete set of momentum vectors in the two-dimensional plane of the cavity. The energy scale $E_\rho = \pi^2 \rho_{2D} \hbar^2 / 2m$ is defined in terms of the molecular density ρ_{2D} and effective photon mass m . The total number of photon modes is truncated to N_{ph} . The light-matter coupling is given by the coupling constant $g_{n,\mathbf{k}} = e^{-i\mathbf{k} \cdot \mathbf{r}_n} \Omega_R / \sqrt{N_m}$, where \mathbf{r}_n is the position of the n th molecule. These plane-wave cavity modes correspond to considering periodic boundary conditions. Coupling of the electronic levels to vibrational modes results in broadening of emission and absorption spectra and in the occurrence of a Stokes shift, which is parametrized by the Huang-Rhys factor S [40]. In later discussions it will be useful to use the notation $(n - m)$ to denote transitions between the n th vibrational ground state and the m th vibrational excited state [see Figs. 1(c) and 1(d)]. The total number of vibrational states on each molecule will be truncated to N_v .

The incoherent processes that occur can be described by the Lindblad formalism. The equation of motion for the density matrix of the system reads as

$$\partial_t \rho = -i[H, \rho] + \sum_{\mathbf{k}} \kappa \mathcal{L}[a_{\mathbf{k}}] + \sum_n (\Gamma_\uparrow \mathcal{L}[\sigma_n^+] + \Gamma_\downarrow \mathcal{L}[\sigma_n^-] + \Gamma_z \mathcal{L}[\sigma_n^z] + \gamma_\uparrow \mathcal{L}[b_n^\dagger + \sqrt{S} \sigma_n^z] + \gamma_\downarrow \mathcal{L}[b_n + \sqrt{S} \sigma_n^z]), \quad (2)$$

with $\mathcal{L}[X] = X \rho X^\dagger - \frac{1}{2}(X^\dagger X \rho + \rho X^\dagger X)$. The equations account for cavity loss at rate κ , dephasing of the excitons Γ_z , and incoherent pumping and decay of excitons with rates Γ_\uparrow and Γ_\downarrow , respectively.¹ The last two terms describe thermal relaxation and excitation with rates $\gamma_\downarrow = \gamma_v (n_b + 1)$ and $\gamma_\uparrow = \gamma_v n_b$ where $n_b = [\exp(\omega_v / k_B T_v) - 1]^{-1}$ is the Bose-Einstein distribution at temperature T_v . The values of all parameters used for the simulations below are given in Table I.

B. Second-order cumulant equations

The size of Hilbert space for N_m molecules, each with $2N_v$ internal states, is too large to directly simulate except for small N_m . To make the simulation computationally tractable for realistic system sizes, we proceed from Eq. (2) by using the second-order cumulant expansion. This provides a (closed) set

¹We note that compared to our previous work [36] we have corrected the sign of the $\sqrt{S} \sigma_n^z$ term in Eq. (2). This does not significantly change the results.

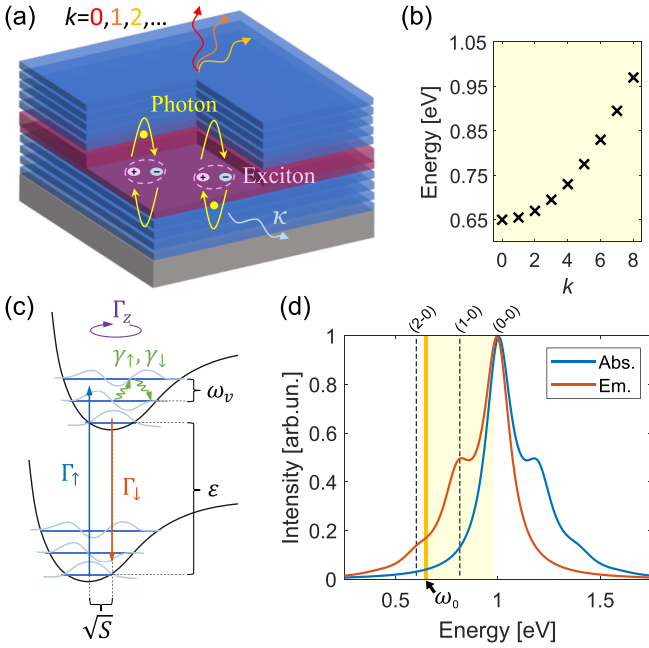


FIG. 1. Schematics of the system and model. (a) A planar microcavity with multiple photon modes and a layer of emitter material. The cavity modes have in-plane momentum k and they decay by rate κ . The photons in the cavity modes can strongly couple to the excitons, hybridizing to form exciton-polaritons. (b) Discretized dispersion relation of the uncoupled cavity modes. (c) Two-level system with both ground and excited states dressed by N_v vibrational states. The bare transition energy between the two electronic states is denoted by ϵ , the vibrational frequency by ω_v , and the Huang-Rhys factor by S . The rates of the drive and dissipation processes involved are the external pumping Γ_\uparrow , spontaneous decay Γ_\downarrow , dephasing Γ_z , and thermal excitation and dissipation of the vibrational modes $\gamma_{\uparrow,\downarrow}$. (d) Absorption and emission spectra of the uncoupled emitters. The yellow shaded area corresponds to the energy range which the uncoupled photon modes cover, starting from ω_0 (0.65 eV). The zero-phonon line (0-0) and the emission shoulders related to the two first vibrational transitions (1-0), (2-0) are labeled.

of equations of motion for first- and second-order correlations between molecule and photon operators [36,41,42].

TABLE I. Simulation parameters.

Parameter	Value	Notes
N_m	10^8	
N_v	4	
N_{ph}	9	
ϵ	1 eV	
ω_0	0.65 eV	$-2\omega_v < \omega_0 - \epsilon < -\omega_v$
E_ρ	5×10^5 eV	
Ω_R	0.1 eV and 0.4 eV	
ω_v	0.2 eV	
S	0.10	
κ	10^{-4} eV	$\sim (40 \text{ ps})^{-1}$
Γ_\downarrow	10^{-4} eV	$\sim (40 \text{ ps})^{-1}$
Γ_z	0.03 eV	$\sim (1 \text{ ps})^{-1}$
γ_v	0.02 eV	
$k_B T_v$	0.025 eV	Room temperature

In order to make the cumulant expansion, it is helpful to first relabel the molecular degrees of freedom. The two electronic states (σ) and the N_v vibrational states (b) are combined into $2N_v$ -level operators, which can be represented by generalized Gell-Mann matrices λ (see Appendix A for details). The Hamiltonian then becomes

$$H = \sum_{\mathbf{k}} \omega_{\mathbf{k}} a_{\mathbf{k}}^\dagger a_{\mathbf{k}} + \sum_n \left[A_i + \sum_{\mathbf{k}} (B_i a_{\mathbf{k}}^\dagger e^{-i\mathbf{k}\cdot\mathbf{r}_n} + \text{H.c.}) \right] \lambda_i^{(n)}, \quad (3)$$

where the vectors A_i and B_i include the terms in Eq. (1). Tensor sums that run over Gell-Mann operator indices i are implicit. In the new basis, the master equation in Eq. (2) takes the form

$$\partial_t \rho = -i[H, \rho] + \sum_{\mathbf{k}} \kappa \mathcal{L}[a_{\mathbf{k}}] + \sum_{\mu, n} \mathcal{L}[\gamma_i^\mu \lambda_i^{(n)}], \quad (4)$$

where μ labels the drive and dissipation processes related to molecules: (1) pump, (2) decay, (3) dephasing, and vibrational (4) excitation and (5) decay.

We next write equations of motion for first- and second-order correlations of the operators $\lambda_i^{(n)}$, $a_{\mathbf{k}}$, $a_{\mathbf{k}}^\dagger$. To produce a closed set of equations of motion, all third- or higher-order correlations are split into products of first- and second-order correlations, by setting third-order cumulants (e.g., $\langle ABC \rangle_c$) to zero. This allows to decompose the third-order terms as $\langle ABC \rangle = \langle A \rangle \langle BC \rangle + \langle B \rangle \langle AC \rangle + \langle C \rangle \langle AB \rangle$ [43]. To further simplify the derivation, we make use of the conservation of number of excitations implied by the RWA and divide the operators λ_i into three groups that either increase (+), decrease (−), or conserve (z) the electronic excitations. With this classification, expectation values of operators that do not conserve the number of excitations can be taken zero, such as the first-order terms $\langle a_{\mathbf{k}} \rangle$, $\langle a_{\mathbf{k}}^\dagger \rangle$, $\langle \lambda_{i-} \rangle$, $\langle \lambda_{i+} \rangle$.

Assuming a spatially homogeneous distribution (or random distribution with a large number) of emitters in the microcavity, we may approximate summation over sites by using $\sum_n e^{i(\mathbf{k}-\mathbf{k}')\cdot\mathbf{r}_n} = N_m \delta_{\mathbf{k},\mathbf{k}'}$, allowing the use of momentum conservation. For the number-conserving Gell-Mann operators we then obtain a site-independent form $\ell_i = \langle \lambda_{i_z}^{(n)} \rangle$. For the two other groups of Gell-Mann operators, $\lambda_{i_+}^{(n)}$ and $\lambda_{i_-}^{(n)}$, the first-order expectations are zero as they do not conserve the number of excitations. We can write the Fourier components of the second-order correlations as $d_{ij}^{\mathbf{k}} = \sum_{n,m \neq n} e^{i\mathbf{k}\cdot(\mathbf{r}_n - \mathbf{r}_m)} \langle \lambda_{i_+}^{(n)} \lambda_{i_-}^{(m)} \rangle / N_m^2$ and $c_i^{\mathbf{k}} = \sum_n e^{i\mathbf{k}\cdot\mathbf{r}_n} \langle a_{\mathbf{k}} \lambda_{i_+}^{(n)} \rangle / N_m$. Photon mode occupations are denoted by $n^{\mathbf{k}} = \langle a_{\mathbf{k}}^\dagger a_{\mathbf{k}} \rangle$. The equations of motion for the nonvanishing correlations are thus

$$\begin{aligned} \partial_t n^{\mathbf{k}} &= -\kappa n^{\mathbf{k}} - 2N_m \text{Im} B_i c_i^{\mathbf{k}}, \\ \partial_t \ell_i &= \xi_{ij} \ell_j + \phi_i - 8 \text{Re} \beta_{ij} \sum_{\mathbf{k}} c_j^{\mathbf{k}}, \\ \partial_t c_i^{\mathbf{k}} &= \left[X_{ij} - \left(i\omega_{\mathbf{k}} + \frac{\kappa}{2} \right) \delta_{ij} \right] c_j^{\mathbf{k}} + 2\beta_{ij}^* \ell_j n_{\mathbf{k}} - i B_j d_{ij}^{\mathbf{k}} \\ &\quad - \frac{i}{N_m} \left(\xi_{ij} \ell_j + \frac{B_i}{2N_v} \right), \\ \partial_t d_{ij}^{\mathbf{k}} &= X_{ip}^* d_{pj}^{\mathbf{k}} + X_{jp} d_{ip}^{\mathbf{k}} + 2\ell_p (\beta_{ip} \tilde{c}_j^{\mathbf{k}*} + \beta_{jp}^* \tilde{c}_i^{\mathbf{k}}), \end{aligned} \quad (5)$$

where $\tilde{c}_i^{\mathbf{k}} = c_i^{\mathbf{k}} - \sum_{\mathbf{q}} c_i^{\mathbf{q}}/N_m$, and the coefficients are given in Appendix A. Equations (5) describe the time evolution of the strongly coupled system with multiple photon modes, capturing the effect of fluctuations. Solving these equations yields the time evolution of the photon mode populations, discussed in Sec. III.

C. Photoluminescence and gain spectra

When coupling between the cavity modes and the emitters is strong, polariton lasing replaces photon lasing. In this limit, understanding the nature of mode competition becomes more challenging since both the gain profile and the normal-mode energies must be found self-consistently, and change with pump strength. In this section we present the numerical approach we will use to extract both quantities, as used in Sec. IV.

The energies of the polariton modes can be found by computing the photoluminescence spectrum, which is given by

$$S_{\mathbf{k}}(\nu) = \int_{-\infty}^{\infty} dt \langle a_{\mathbf{k}}^{\dagger}(t) a_{\mathbf{k}}(0) \rangle e^{i\nu t}. \quad (6)$$

Here, we utilize the quantum regression theorem to calculate the two-time correlators [44]. Solving $S_{\mathbf{k}}(\nu)$ requires the steady-state density matrix ρ_{ss} which is used to construct $\tilde{\rho}_{\mathbf{k}}(0) = a_{\mathbf{k}} \rho_{ss}$. Time evolving the effective density matrix $\tilde{\rho}_{\mathbf{k}}(t) = e^{t\mathcal{L}} \tilde{\rho}_{\mathbf{k}}(0)$ and evaluating $\text{Tr}[a_{\mathbf{k}}^{\dagger} \tilde{\rho}_{\mathbf{k}}(t)]$ gives the coupled differential equations for the two-time correlators [45]:

$$\begin{aligned} \partial_t \langle a_{\mathbf{k}}^{\dagger}(t) a_{\mathbf{k}}(0) \rangle &= \left(i\omega_{\mathbf{k}} - \frac{\kappa}{2} \right) \langle a_{\mathbf{k}}^{\dagger}(t) a_{\mathbf{k}}(0) \rangle + iN_m B_i^* c_i^{\mathbf{k}}(t), \\ \partial_t c_i^{\mathbf{k}}(t) &= \xi_{ij} c_j^{\mathbf{k}}(t) + 2f_{ijp} B_j \ell_p \langle a_{\mathbf{k}}^{\dagger}(t) a_{\mathbf{k}}(0) \rangle, \end{aligned} \quad (7)$$

where $c_i^{\mathbf{k}}(t) = \frac{1}{N_m} \sum_n e^{i\mathbf{k}\cdot\mathbf{r}_n} \text{Tr}[\lambda_{i+}^{(n)} \tilde{\rho}_{\mathbf{k}}(t)]$ and

$$\langle a_{\mathbf{k}}^{\dagger}(t) a_{\mathbf{k}}(0) \rangle = \text{Tr}[a_{\mathbf{k}}^{\dagger} e^{t\mathcal{L}} a_{\mathbf{k}} \rho_{ss}].$$

In the steady state, ℓ_p becomes constant. The linear equations can be written in a matrix form as $\partial_t \mathbf{C}_{\mathbf{k}} = \mathcal{M} \mathbf{C}_{\mathbf{k}}$, where the vector $\mathbf{C}_{\mathbf{k}} = [\langle a_{\mathbf{k}}^{\dagger}(t) a_{\mathbf{k}}(0) \rangle, \{c_i^{\mathbf{k}}(t)\}_i]$ and the matrix \mathcal{M} are obtained from Eqs. (7). The Fourier transform can be written as

$$\begin{aligned} S_{\mathbf{k}}(\nu) &= \int_{-\infty}^{\infty} e^{i\nu t + \mathcal{M}t} \mathbf{C}(0) dt \\ &= (i\nu + \mathcal{M})^{-1} \mathbf{C}(0) = \sum_i \frac{\alpha_i}{\mu_i + i\nu} |r_i\rangle, \end{aligned} \quad (8)$$

where μ_i is the eigenvalue of \mathcal{M} that corresponds to the right $|r_i\rangle$ and left $\langle l_i|$ eigenvectors. The coefficient α_i is then given by $\alpha_i = \langle l_i | \mathbf{C}(0) \rangle / \langle l_i | r_i \rangle$.

The ‘‘gain’’ (i.e., emission minus absorption) can be studied by considering two-time correlations of the molecules:

$$\begin{aligned} G(\nu) &= \int_{-\infty}^{\infty} dt e^{-i\nu t} \langle [\sigma^{+(n)}(t), \sigma^{-(n)}(0)] \rangle \\ &= V_i^+ V_j^- \int_{-\infty}^{\infty} dt e^{-i\nu t} \langle [\lambda_i^{(n)}(t), \lambda_j^{(n)}(0)] \rangle, \end{aligned} \quad (9)$$

where $V_i^{\pm} = \frac{1}{2} \text{Tr}(\sigma^{\pm} \lambda_i)$. In the weak-coupling picture, this has a simple interpretation as the frequency-resolved gain the

photon modes see; at strong coupling the picture is more complicated, but this nonetheless allows one to probe the molecular dynamics separately from the photons.

By also considering the time-dependent correlations between different molecules, one can further compute the momentum-resolved gain spectrum:

$$\begin{aligned} G_{\mathbf{k}}(\nu) &= V_i^+ V_j^- \int_{-\infty}^{\infty} dt e^{-i\nu t} \\ &\times \sum_{n,m} e^{i\mathbf{k}\cdot(\mathbf{r}_n - \mathbf{r}_m)} \langle [\lambda_i^{(n)}(t), \lambda_j^{(m)}(0)] \rangle. \end{aligned} \quad (10)$$

This quantity identifies the different gain seen by each cavity mode, and so helps explain when mode switching occurs. Note that we can recover the form of $G(\nu)$ in Eq. (9) by summing $G_{\mathbf{k}}(\nu)$ over all \mathbf{k} .

III. MULTIMODE LASING DYNAMICS WITH CONTINUOUS PUMP

A. Weak-coupling regime

Using the methods described in the previous section, we now explore the dynamics of mode switching, starting with the weak-coupling regime, for which we set $\Omega_R = 0.1$ eV. As shown in Figs. 2(a) and 2(b) (similar results also seen in our previous work [36]), for the parameters we use the lasing mode switches between $k = 5$ and 0 as a function of pump strength. Upon increasing the pump strength, the mode $k = 5$, which is closest to resonance with the $(1 - 0)$ transition, starts lasing first. When the pump is further increased, the $k = 0$ starts to lase, and the lasing at $k = 5$ is suppressed. As noted in Ref. [36], the selection of which mode wins mode competition in the weak-coupling regime can be understood by considering the different thresholds and gradients of input-output curves (photon population vs pump power) of these modes. The modes near the vibrational shoulder ($k = 4, 5, 6$) have the lowest threshold pump power, but the mode near $k = 0$ has the highest gradient. If one extrapolates the input-output curves of the different lasing modes beyond the range of values of power where they are lasing, these extrapolated curves will cross at a pump power. (The fact they cross is inevitable when the mode with lower threshold has a lower gradient.) As was shown in Ref. [36] the point where these extrapolated curves cross is the point where switching occurs. As such, one may associate this switching with the differences in thresholds and gradients of the input-output curves.

The time evolution of the system, as shown in Figs. 2(c)–2(k), reveals that mode switching occurs not only as a function of pump strength, but also in time. Here, the term ‘‘switching’’ corresponds to the time instant when the population of one lasing mode surpasses the population of another mode. Figures 2(c), 2(f), and 2(i) show for illustrative purpose the data shown in Figs. 2(d), 2(g), and 2(j), which presents the population of selected k modes. Figures 2(e), 2(h), and 2(k) show the population inversion as a function of time.

At a low pump strength, in Figs. 2(c) and 2(d), lasing starts and remains at $k = 5$ until steady state is reached. At higher pump strengths, as shown in Figs. 2(f) and 2(g) and 2(i) and 2(j), switching to $k = 0$ mode occurs. At a high pump strength [Figs. 2(i) and 2(j)], lasing at $k = 0$ completely suppresses the

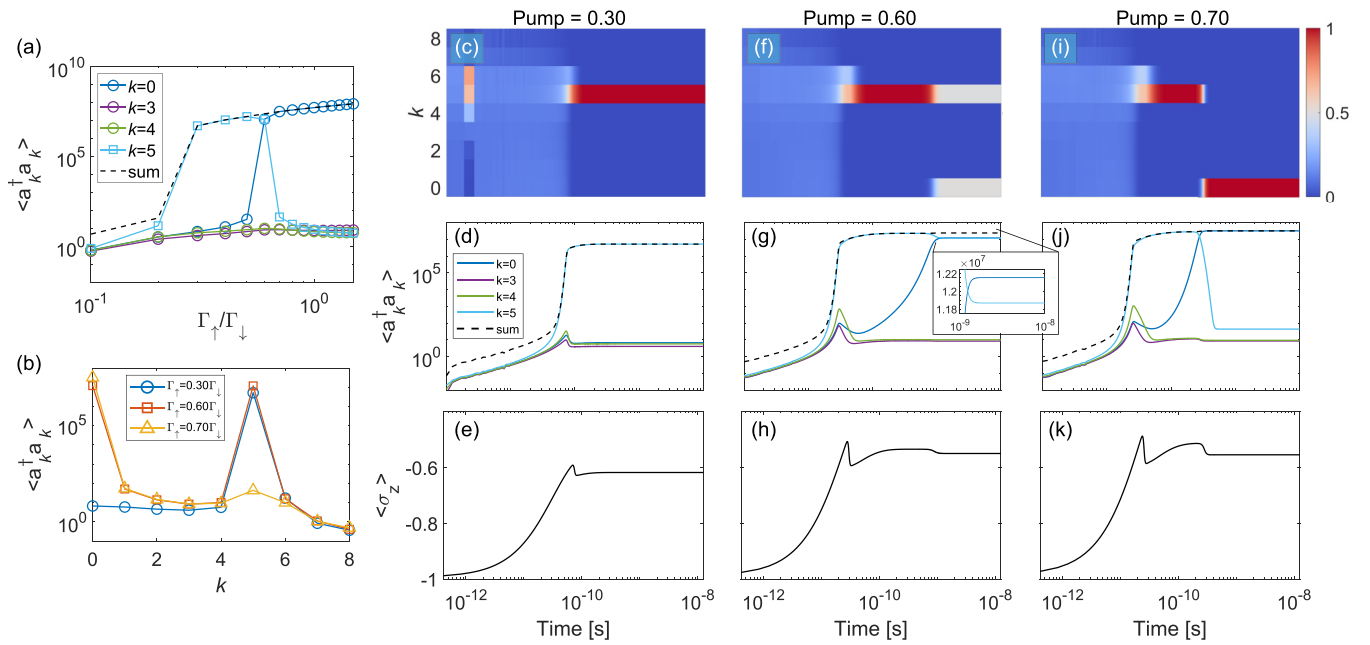


FIG. 2. Mode competition for weak coupling, $\Omega_R = 0.1$ eV. (a) Pump dependence curves and (b) steady-state occupations at different k modes. The mode occupations in (b) are shown for selected pumps. The time-integrated threshold curves are shown in Appendix B. On the right: (top and middle rows) time evolution of photon population at different modes and (bottom row) population inversion of the two-level system as a function of pump strength. The pump strengths are (c)–(e) $\Gamma_\uparrow/\Gamma_\downarrow = 0.30$, (f)–(h) 0.60, and (i)–(k) 0.70. All other parameters are provided in Table I.

lasing at $k = 5$ after the switch. Only in a very narrow range of pump strengths, as illustrated in Figs. 2(f) and 2(g), does the system show bimodal lasing. In that case, the $k = 0$ mode slowly grows until it marginally prevails, and both modes sustain a macroscopic population at steady state. The dashed lines in Figs. 2(d), 2(g), and 2(j) show the photon population summed over all k modes. It is interesting to note that the sum over all k modes shows only a single threshold; whenever switching takes place the photon population is redistributed between different modes. One may note also that the population inversion [as shown in Figs. 2(e), 2(h), and 2(k)] appears to reach a stationary value before switching occurs. After the switch, the inversion does, however, show a small kink. In Fig. 3, we show the rate at which the metastable $k = 5$ state is replaced by $k = 0$. We see that the rate vanishes as one approaches the transition point, i.e., the pump strength where bimodal lasing is observed [$\sim 0.6\Gamma_\downarrow$, Figs. 2(f)–2(h)].

B. Strong-coupling regime

At strong coupling ($\Omega_R = 0.4$ eV) we observe shifting of the lasing mode towards higher k on increasing the pump strength. As shown by the threshold curves and spectra in Figs. 4(a) and 4(b), lasing is first triggered in the $k = 5$ mode but switches to $k = 7$ at high pump strengths. In a narrow regime of pump strengths, the $k = 6$ mode has the highest occupation.

The time evolution of the mode occupations for strong coupling is presented in Figs. 4(c)–4(k). At a low pump strength, in Figs. 4(c) and 4(d), lasing starts at $k = 5$ and switches to a lower $k = 4$ mode. At higher pump strengths, in Figs. 4(f) and 4(g) and 4(i) and 4(j), the lasing mode switches to higher

k modes. One notable distinction from weak coupling is seen in the time evolution of the population inversion. As seen in Figs. 4(h) and 4(k), the population inversion continues to grow until the (final) mode switching occurs.

Both in the strong- and weak-coupling regimes, we have referred to the lasing modes with the absolute value of the momentum vector $k = |\mathbf{k}|$. Within our model, as we have no source of disorder, all modes with a given $|\mathbf{k}|$ are degenerate. In real experiments, the disorder that will be present is likely to break the perfect degeneracy, leading to a particular angular pattern being selected for the lasing mode.

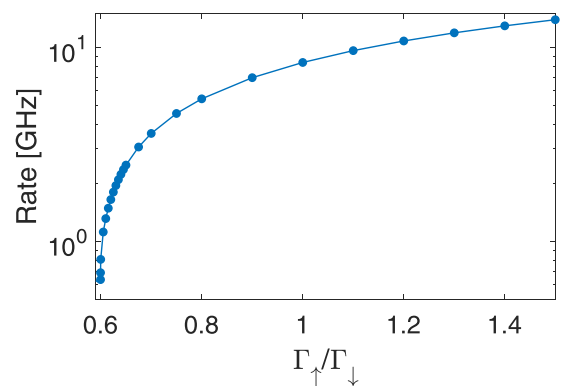


FIG. 3. Metastable decay rate of the $k = 5$ mode as a function of pump strength, in the vicinity of the transition point. The decay rate is the inverse of the time at which the lasing mode switch occurs, i.e., when the population of mode $k = 0$ exceeds that of mode $k = 5$. Parameters as in Fig. 2.

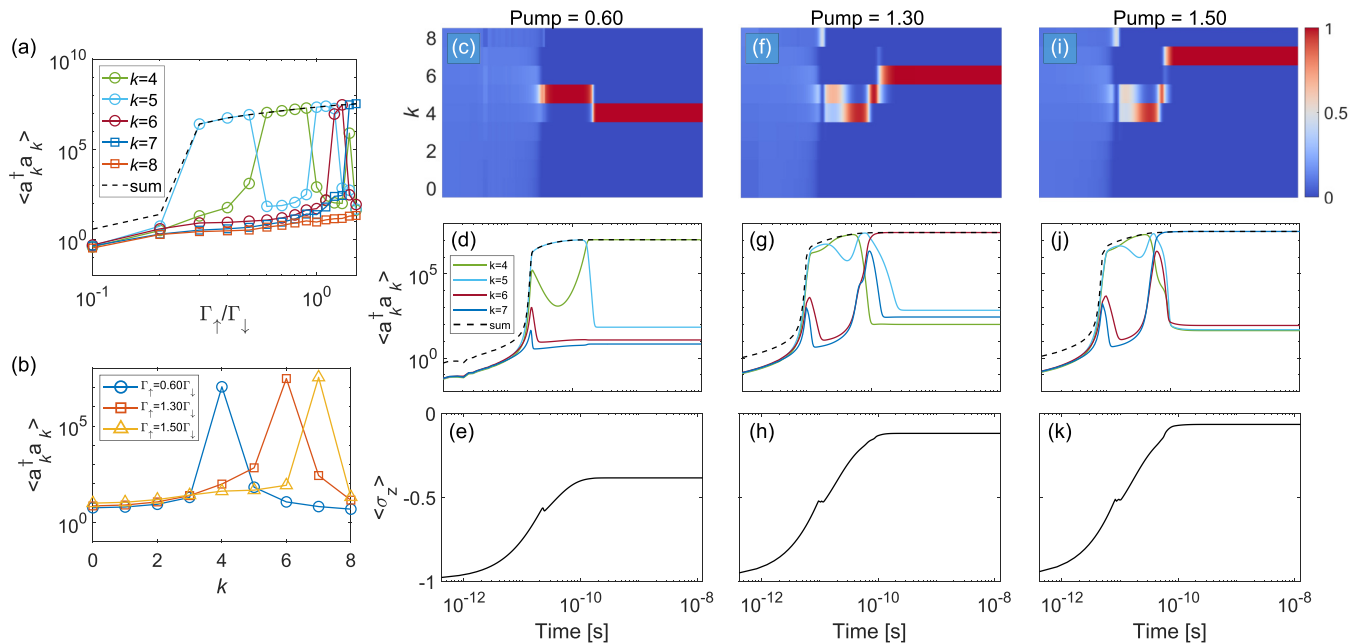


FIG. 4. Mode competition for strong coupling, $\Omega_R = 0.4$ eV. (a) Pump dependence curves and (b) steady-state occupations at different k modes. The mode occupations in (b) are shown for selected pumps. The time-integrated threshold curves are shown in Appendix B. (Top and middle rows) Time evolution of photon population at different modes and (bottom row) population inversion of the two-level system as a function of pump strength. The pump strengths are (c)–(e) $\Gamma_\uparrow/\Gamma_\downarrow = 0.60$, (f)–(h) 1.30, and (i)–(k) 1.50. All other parameters are provided in Table I.

IV. GAIN SPECTRUM

To better understand why mode switching occurs in response to pumping, we next discuss how gain and photoluminescence spectra change as a function of pump power. To avoid the subtleties associated with time-dependent spectra [46], we only consider the steady-state spectra.

A. Weak-coupling regime

To introduce the properties of the gain spectrum, we start by considering the total (momentum-integrated) spectrum $G(\nu)$ of the molecules defined in Eq. (9). Figure 5 shows $G(\nu)$ for weak coupling, at a narrow range of pump strengths (see legend) near the initial lasing threshold ($\sim 0.21 \Gamma_\uparrow/\Gamma_\downarrow$). Since $G(\nu)$ can be either positive (net gain from the molecules) or negative (net absorption), we show both $G(\nu)$ and $-G(\nu)$ on logarithmic scales. Below threshold (dashed lines) $G(\nu)$ is negative at all frequencies. As the pump strength increases, a region of positive gain develops. Positive gain from the molecules does not immediately lead to lasing, as it is not sufficient to overcome the cavity losses. When the gain at the frequency of the $k = 5$ cavity mode (around 0.75 eV) becomes sufficiently high to exceed cavity loss, lasing occurs. Figure 6 then shows how the gain spectrum continues to develop, considering a wider range of frequencies (covering all relevant cavity modes) and a wider range of pump strengths. From this figure, one sees that between pump strengths 0.60 and 0.70 $\Gamma_\uparrow/\Gamma_\downarrow$ the peak of the gain switches to a lower-energy mode at 0.63–0.64 eV.

We can further study how the gain affects different cavity modes by considering $G_k(\nu)$. The momentum-resolved gain

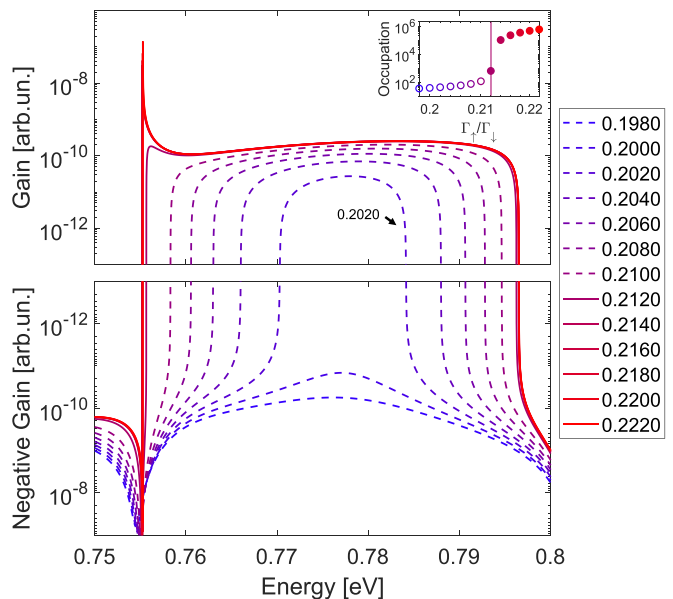


FIG. 5. Momentum-integrated gain spectra $G(\nu)$ near the lasing threshold for weak coupling, $\Omega_R = 0.1$ eV. The top panel shows $G(\nu)$, while the bottom panel shows $-G(\nu)$, both on a logarithmic scale. The pump strengths are color coded as in the legend and the inset which shows the corresponding part of the threshold curve. Solid lines in the panels (and filled circles in the inset) are results above the lasing threshold, while dashed lines are below threshold. Threshold, which requires gain to exceed the cavity losses occurs around $0.21 \Gamma_\uparrow/\Gamma_\downarrow$, is marked by the vertical line in the inset. All other parameters as in Table I.

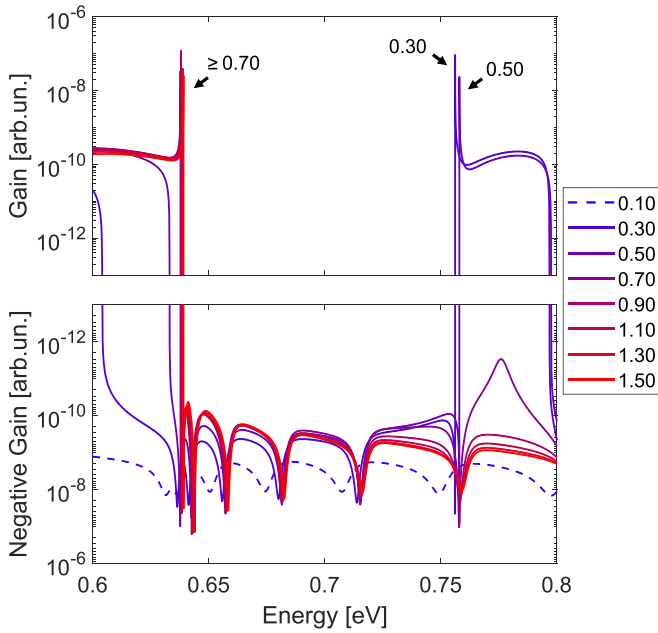


FIG. 6. Momentum-integrated gain spectra $G(\nu)$ as a function of pump strength for the weak-coupling case $\Omega_R = 0.1$ eV. This figure shows an expanded range of energies and pump strengths compared to Fig. 5.

spectra are shown in Figs. 7(a)–7(c) for the three selected pumps that were studied in Sec. III (Fig. 2). Here only the positive gain values are plotted. The results confirm that the peak of the gain shifts from the mode $k = 5$ to 0 as the pump is increased, and there is a narrow region of pump strengths where the gain is similar for the two modes. We calculated also the photoluminescence spectrum $S_k(\nu)$ to see how the mode energies change upon increasing the pump strength. As shown in Figs. 7(d)–7(f), under weak coupling the modes are only slightly shifted from the bare photon dispersion, and so in this case the mode locations remain practically unchanged as the pump is increased.

B. Strong-coupling regime

In the strongly coupled system one should now consider lasing arising from scattering into the polariton modes. As discussed elsewhere [39,47], one can still consider a gain spectrum for feeding into the polariton mode. This gain spectrum corresponds to the reservoir of dark excitonic states. At strong coupling, the gain spectrum shows more complex changes as a function of pump strength. Figure 8 shows the evolution of total gain $G(\nu)$ with pump strength. At pump strengths far below threshold the gain is always negative, while above threshold one sees various regions with net gain (i.e., gain exceeding cavity loss), with peaks that indicate lasing. As pumping is further increased, the net gain moves

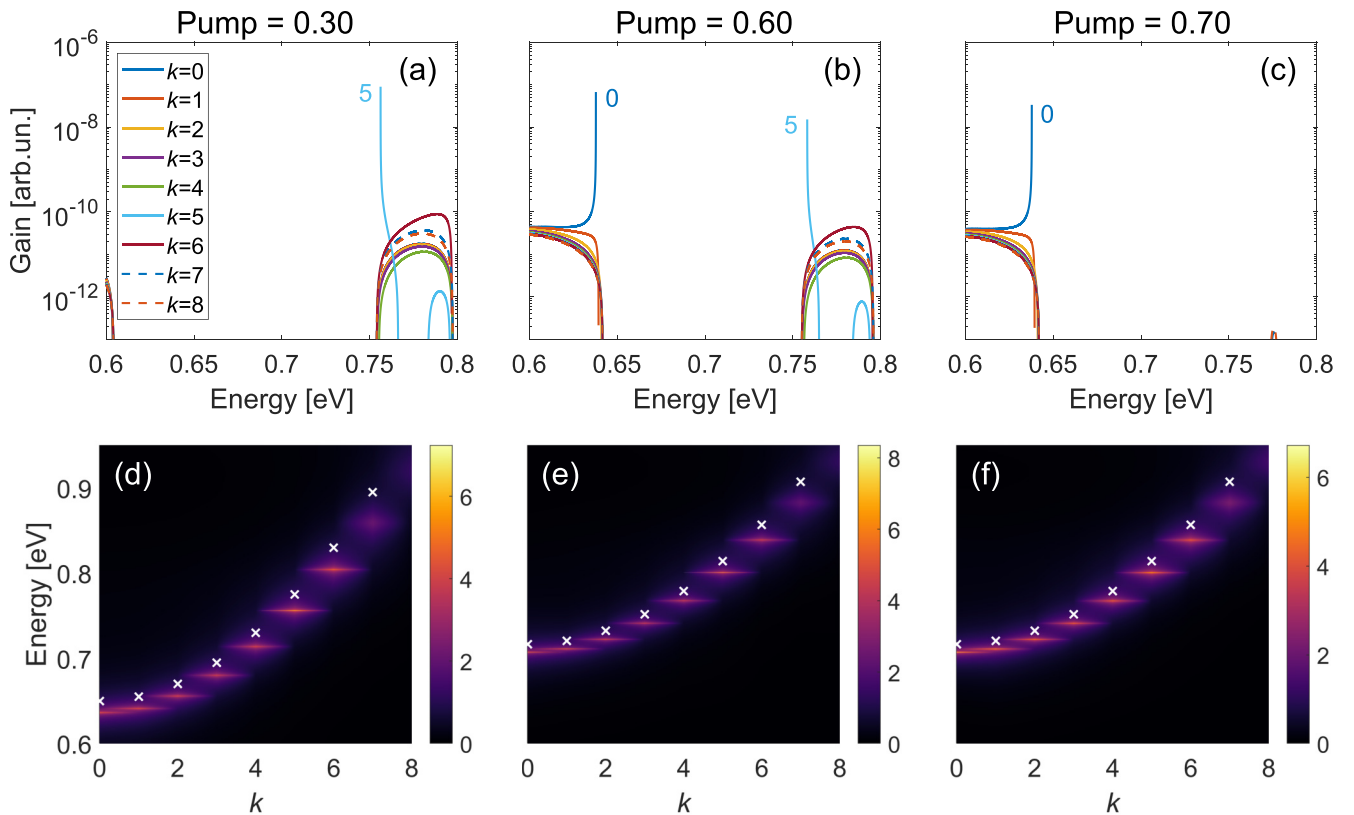


FIG. 7. (a)–(c) Momentum-resolved gain spectra $G_k(\nu)$ and (d)–(f) photoluminescence spectra $S_k(\nu)$ for selected pump strengths for the weak-coupling case $\Omega_R = 0.1$ eV. In (a)–(c) the numbers next to the peaks label the k of the mode(s) that are lasing in the steady state. In (d)–(f) the white crosses mark the uncoupled cavity modes. The pump strengths are (a), (d) $0.30 \Gamma_{\uparrow}/\Gamma_{\downarrow}$, (b), (e) $0.60 \Gamma_{\uparrow}/\Gamma_{\downarrow}$, and (c), (f) $0.70 \Gamma_{\uparrow}/\Gamma_{\downarrow}$; all other parameters as in Table I.

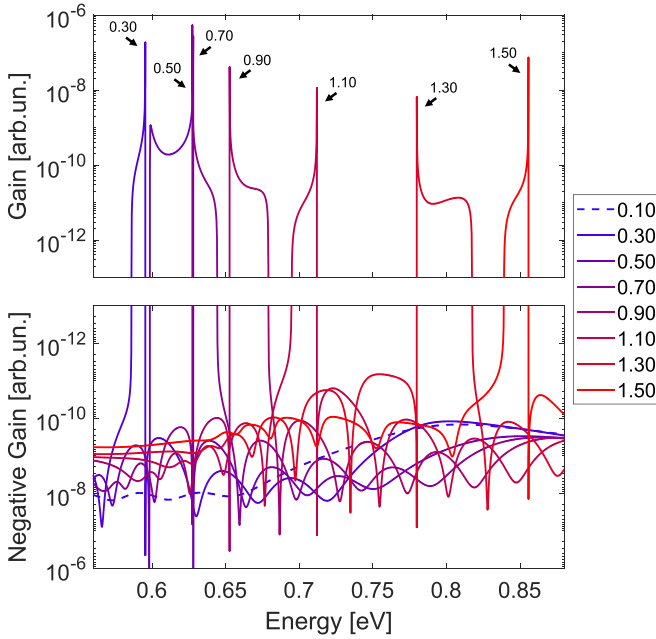


FIG. 8. Total gain spectra $G(\nu)$ as a function of pump strength for strong coupling, $\Omega_R = 0.4$ eV. As in Figs. 5 and 6, the two panels show $G(\nu)$ and $-G(\nu)$ on a logarithmic scale. The pump strengths are color coded according to the legend, and all other parameters are as in Table I.

toward higher energies. The shift can be explained by considering two effects that arise due to strong coupling and pumping.

First, gain is increased at higher energies as a result of the vibrational sidebands becoming successively inverted with stronger pumping. To understand this we must consider both the relative populations of the ground and excited electronic manifolds, and the populations of the vibrational sublevels labeled by n as illustrated in Fig. 9. Considering the ground-state electronic manifold, we may state the following about the populations of the sublevels. Unless pumping becomes very strong, the vibrational sublevels will be populated thermally (according to a Boltzmann distribution), so the $n = 0$ sublevel is most populated and the higher n are less populated. Turning now to the population of the electronic excited states, we may note that the population of the excited state manifold is zero at weak pumping and grows with pumping.

Therefore, with increasing pumping the population of the excited-state manifold will start to exceed the populations of the ground-state-manifold sublevels, such that the first sideband to get inverted corresponds to transitions from the 0th state of the excited manifold to the highest n state of the ground-state manifold [the $(n - 0)$ transition] (see Fig. 9). That first inverted transition is also the transition involving the smallest energy difference, thus it leads to gain at lower energies. As the pumping increases further, sidebands with successively smaller n additionally become inverted, thus one starts to get gain at higher energies. At the same time the excited-state sublevels with $m > 0$ can also become inverted. Both these processes mean $(n - m)$ transitions with larger energy difference are inverted, shifting the gain toward higher energy [39].

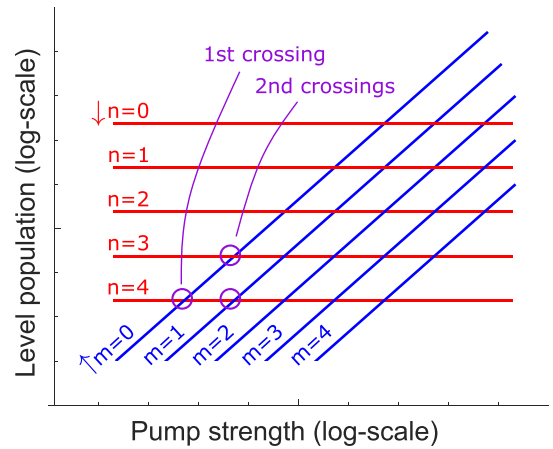


FIG. 9. Schematic cartoon of successive inversion of sublevel transitions when vibrational sublevels are thermally populated. Blue and red solid lines represent the m and n levels for transitions $n - m$ from excited-state manifold (m) to the ground-state manifold (n) of an organic emitter. As pump strength is increased, the first transition to undergo population inversion is the $4 - 0$ transition, which corresponds to transitions from the zeroth state of the excited-state manifold to the fourth state of the ground-state manifold.

The second effect to be considered is that not only the gain, but also the energies of the strongly coupled normal modes evolve with pump strength. As shown by the momentum-resolved results in Figs. 10(a)–10(c), for instance, when the pump strength is increased from 1.30 to 1.50 $\Gamma_{\uparrow}/\Gamma_{\downarrow}$, the gain spectrum moves from 0.78–0.82 eV to 0.84–0.86 eV. The photoluminescence spectra in Figs. 10(d)–10(f) show that the dips associated with the polaritonic mode frequencies move to higher energy as the whole dispersion blueshifts upon increasing pump. The blueshift originates from saturation of the two-level systems [36], reducing the effective coupling strength, ultimately recovering the uncoupled photon mode dispersion at very strong pumping.

Summarizing, the shifting of the lasing mode toward higher energies upon increasing pumping in the strong-coupling case is caused by combined effects of the gain moving toward higher energies, as well as the blueshifting of the polariton mode frequencies.

V. MULTIMODE LASING DYNAMICS WITH PULSED PUMP

Next we consider the case of pulsed excitation, which is relevant for typical experiments on organic exciton-polariton systems. We excite the system with a 4-ps pulse that has a Gaussian time dependence, and study the dynamics of mode switching as a function of pump strength (amplitude). All other parameters are as in Sec. III.

A. Weak-coupling regime

In the weak-coupling regime, at low pump strength [Figs. 11(c) and 11(d)], lasing occurs at $k = 5$ until decay causes lasing to cease. At higher pump strengths, as shown in Figs. 11(f) and 11(g) and 11(i) and 11(j), the lasing mode

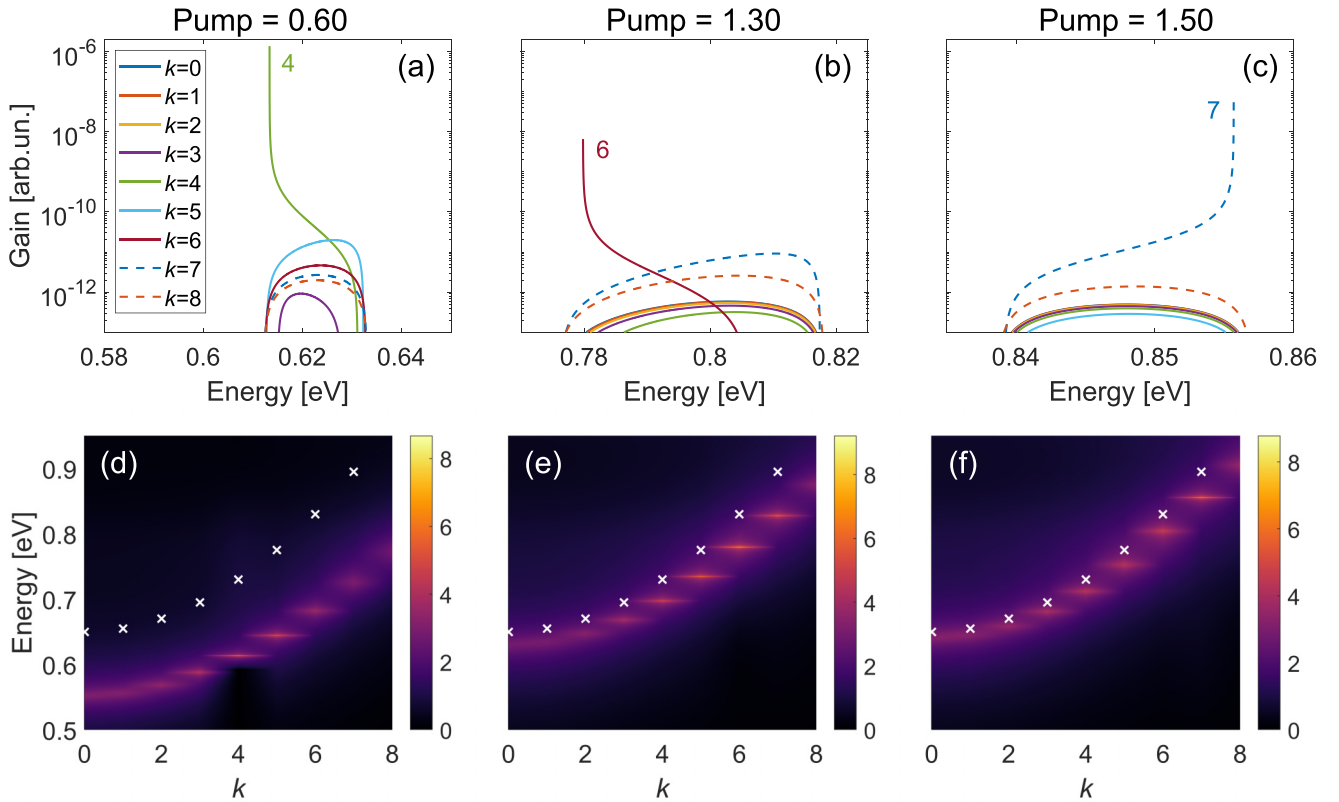


FIG. 10. (a)–(c) Momentum-resolved gain and (d)–(f) photoluminescence spectra for selected pump strengths for the strong-coupling case $\Omega_R = 0.4$ eV. (a)–(c) The numbers next to the gain peaks label the k of the mode(s) that are lasing in the steady state. (d)–(f) The white crosses mark the uncoupled cavity modes. The color scale is logarithmic. The pump strengths are (a), (d) $0.60 \Gamma_\uparrow/\Gamma_\downarrow$, (b), (e) $1.30 \Gamma_\uparrow/\Gamma_\downarrow$, and (c), (f) $1.50 \Gamma_\uparrow/\Gamma_\downarrow$.

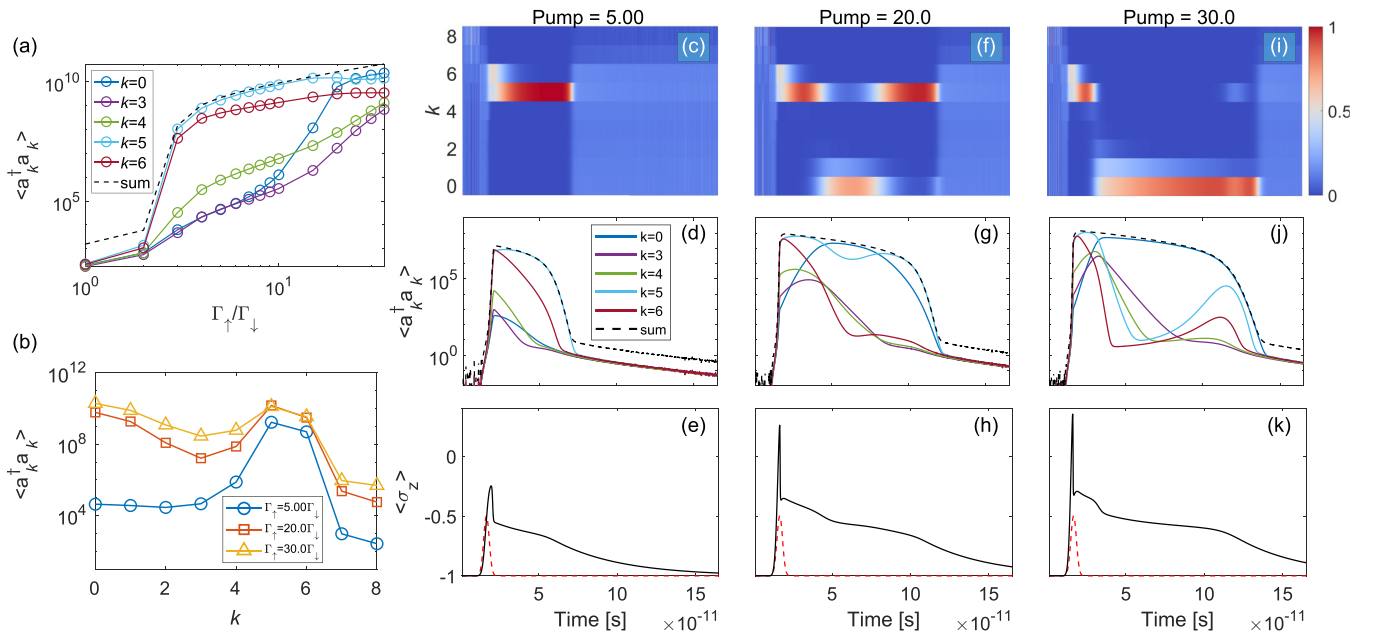


FIG. 11. Mode competition with pulsed excitation for weak coupling, $\Omega_R = 0.1$ eV. (a) Time-integrated pump dependence curves and (b) occupations at different k modes for selected pumps. On the right (c)–(k): (top and middle rows) time evolution of photon population at different modes and (bottom row) population inversion of the two-level system at various pump strengths. The excitation pulse has a Gaussian time dependence centered at around 16 ps with full width at half-maximum of around 4 ps. The pulse profile is shown in (e), (h), and (k) by the red dashed line (in arbitrary units). The peak pump strengths are (c)–(e) $\Gamma_\uparrow/\Gamma_\downarrow = 5.00$, (f)–(h) 20.0, and (i)–(k) 30.0. All other parameters are provided in Table I. Note that here the time axis is in linear scale.

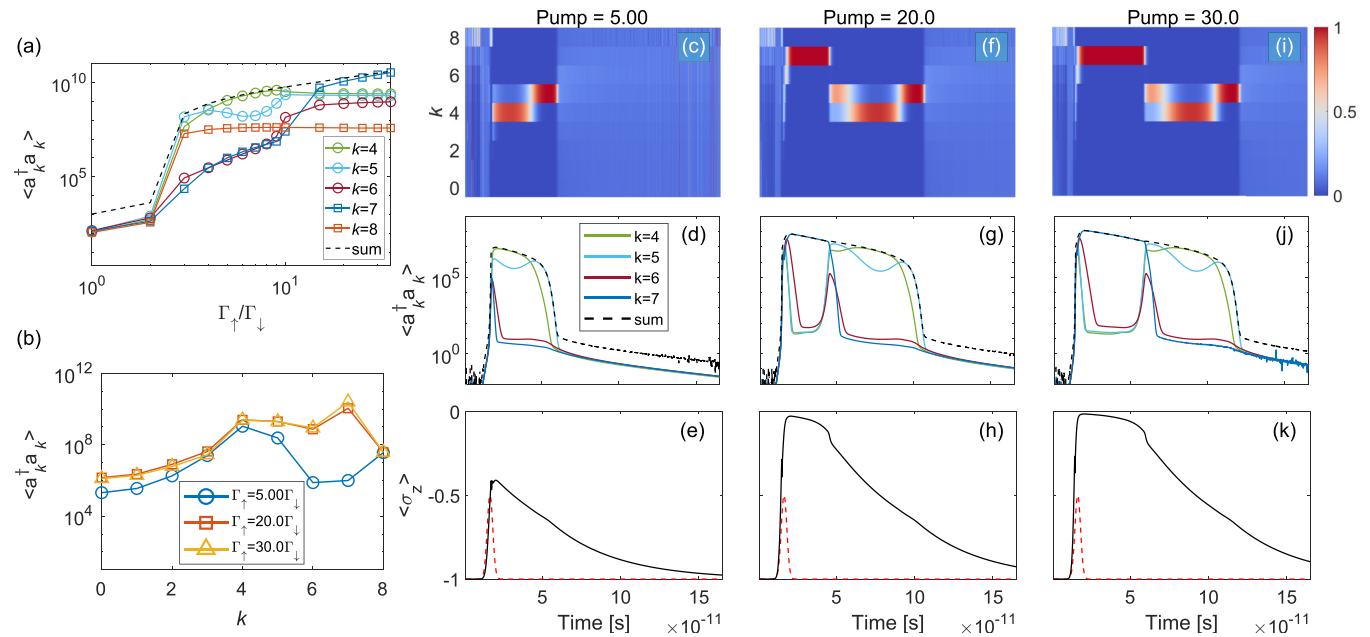


FIG. 12. Mode competition with pulsed excitation for strong coupling, $\Omega_R = 0.4$ eV. (a) Time-integrated pump dependence curves and (b) occupations at different k modes for selected pump powers. On the right (c)–(k): (top and middle rows) time evolution of photon population at different modes and (bottom row) population inversion of the two-level system at various pump strengths. The excitation pulse has a Gaussian time dependence centered at around 16 ps with full width at half-maximum of around 4 ps. The pulse profile is shown in (e), (h), (k) by the red dashed line (in arbitrary units). The peak pump strengths are (c)–(e) $\Gamma_\uparrow/\Gamma_\downarrow = 5.00$, (f)–(h) 20.0, and (i)–(k) 30.0. All other parameters are provided in Table I. Note that here the time axis is in linear scale.

switches from $k = 5$ to 0 similar to the continuous pump case discussed in Sec. III. However, here the lasing mode switches from $k = 0$ back to $k = 5$ as the population decays. Throughout the studied pump range, the higher $k = 6$ mode gains large population at the onset of lasing. This is also visible in the time-integrated threshold curve and populations in Figs. 11(a) and 11(b): occupation of the $k = 6$ mode follows quite closely that of the $k = 5$ mode. As shown by Figs. 11(h) and 11(k), at higher pump strengths the two-level systems have very high inversion before the onset of lasing, which is likely connected to excess gain, enough to trigger lasing in several modes.

As noted above, considering time-dependent gain spectra present some issues with interpretation [46]. The steady-state spectra presented in Sec. IV can, however, provide some intuition on how the gain and photoluminescence might shift under time-dependent population inversion. For example, at weak coupling, the peak of the gain switched from $k = 5$ to 0 mode when the (continuous) pump strength was increased from 0.30 to 0.70. Here in the pulsed case, the lasing peak switches in a qualitatively similar way (both as a function of pump strength as well as in time).

B. Strong-coupling regime

At strong coupling, for pulsed excitation we observe again rich switching dynamics. At low pump strength, as shown in Figs. 12(c) and 12(d), lasing starts at $k = 4$ mode and switches to a higher $k = 5$ mode before the population decays. At higher pump strengths, lasing starts in the high $k = 7$ mode and undergoes switching via $k = 5$ to 4 and back to $k = 5$. The duration of the $k = 7$ lasing coincides with the time that $\langle \sigma_z \rangle$, shown in Figs. 12(h) and 12(k), remains clamped close to

0 by polariton lasing. This duration grows upon increasing the pump strength. The switching sequence to the lower k modes, 5–4–5, occurs during the decay of $\langle \sigma_z \rangle$ in a timescale that we observe to be roughly independent of the pump strength (we confirmed this up to pump amplitude $\Gamma_\uparrow/\Gamma_\downarrow = 150$). This timescale is around 40 ps which corresponds to the decay times of spontaneous emission and cavity modes (Table I).

Similar to the weak-coupling case, for a short time at the onset of lasing, multiple modes are highly occupied, which contributes to the time-integrated populations shown in Figs. 12(a) and 12(b).

VI. DISCUSSION

By simulating the time evolution of the photon population, we have explored the dynamics of mode switching, behavior which could not be seen if only the steady-state result is studied. For example, in Figs. 2(c) and 2(f), the steady-state result would show single-mode ($k = 0$) lasing whereas the time evolution reveals that a higher-energy mode ($k = 5$) is lasing at earlier times. Furthermore, when comparing simulations to experiments dealing with fast dynamics, the experimental measurement is often restricted to observing the time-integrated spectrum, which may lead to incorrect interpretations of the properties of the system (see Appendix B). Especially in experiments with fast pulsed excitation, it is common to record time-integrated spectra. Here we have shown that for pulsed excitation the lasing mode can temporarily switch such that the time-integrated spectra will exhibit several lasing peaks (or a broadened peak with substructure, depending on the mode spacing and resolution of the measurement apparatus). Resolving the time evolution is therefore

important in describing the behavior of such systems both in simulations and in experiments.

From the gain calculations we can generally conclude that lasing occurs at a mode (or modes) where there is a sharp positive peak in the gain spectrum. The results suggest that if several modes have positive gain, the mode with the highest positive gain peak will win out the lasing mode competition. In the weak-coupling case the highest peak in the gain spectrum simply switches from a higher $k = 5$ mode into the $k = 0$ mode, given by the different thresholds and gradients of each mode. In the strongly coupled system, the observed shift of the lasing mode towards higher k modes originates from the shifting of both the gain and the polariton modes toward higher energies as pump is increased.

We believe that observing mode competition effects such as those shown here is realistic in current experiments. In this paper we used a loss rate of 0.1 meV for both the cavity modes and the excitons. This corresponds to lifetimes of ~ 40 ps (see Table I for all simulation parameters). Under continuous pumping, the lasing starts at around $t = 100$ ps ($t = 10$ ps) in the weak- (strong-) coupling case. As shown in Fig. 3, the time that it takes for the mode switching to occur depends strongly on the pump strength. Nevertheless, we can take examples from our data. In the weak- (strong-) coupling case with continuous pumping, at pump strength $\Gamma_{\uparrow}/\Gamma_{\downarrow} = 0.70$ (1.30), the switching occurs at around $t = 1000$ ps ($t = 100$ ps), i.e., after 10 times the time required for lasing to start, or 25 times (2.5 times) the cavity mode lifetime. Another example can be drawn from the pulsed excitation scheme, where the lasing mode is shown to undergo several switching events within 80–120 ps, or 2–3 times the cavity lifetime, from the arrival of the excitation pulse. The temporal switching of lasing modes could be resolved by, e.g., a streak camera.

We note that the cavity lifetime used in the simulations is rather long for an organic polariton system. Cavity lifetimes of the order 10–100 ps are typical for inorganic polariton systems, whereas in organic systems, the lifetimes are typically in the picosecond scale [13]. The choice of simulation parameters in this study is based on our earlier works [36,39], and we stress here that the results are similar for shorter lifetimes.

Multimode polariton lasing could potentially be of use for technological applications. Mode switching phenomena could be used in optical information processing in a similar fashion as polariton switches [48,49] and transistors [50,51] (based on on and off switching of the output intensity of a single-mode condensate) have been proposed. Furthermore, when a system is at a point where multiple modes are lasing in the steady state, even a small disturbance in the operating conditions may push the system from one configuration to another, which could be utilized in sensing applications.

The research data underpinning this publication can be accessed at [52].

ACKNOWLEDGMENTS

A.J.M. and P.T. acknowledge support by the Academy of Finland under Projects No. 303351, No. 307419, No. 327293, No. 318987 (QuantERA project RouTe), No. 318937

(PROFI), and No. 320167 (Flagship Programme, Photonics Research and Innovation (PREIN)), and by Centre for Quantum Engineering (CQE) at Aalto University. A.J.M. acknowledges financial support by the Jenny and Antti Wihuri Foundation and ETH Zurich Postdoctoral Fellowship. K.B.A. and J.K. acknowledge financial support from EPSRC program ‘‘Hybrid Polaritonics’’ (Grant No. EP/M025330/1). K.B.A. acknowledges support from The RSE Saltire Research Award.

APPENDIX A: DETAILS OF GENERALIZED GELL-MANN MATRICES

In this Appendix we provide mathematical details of the generalized Gell-Mann matrix representation of the molecules. Gell-Mann matrices which have previously been used, e.g., in describing the strong interaction in particle physics [53,54]. Their commutation and product rules are given by

$$\begin{aligned} \lambda_i &= \lambda_i^\dagger, & \text{Tr} \lambda_i &= 0, & \text{Tr}[\lambda_i \lambda_j] &= \delta_{ij}, \\ [\lambda_i, \lambda_j] &= 2if_{ijk}\lambda_k, & \lambda_i \lambda_j &= \zeta_{ijk}\lambda_k + \frac{2}{N_\lambda} \delta_{ij}, \end{aligned}$$

where we may write $\zeta_{ijk} = if_{ijk} + t_{ijk}$ and N_λ is the dimension of the matrices. The tensors f_{ijk} and t_{ijk} are the symmetric and antisymmetric structure constants, respectively. Gell-Mann matrices allow for expanding any linear $N_\lambda \times N_\lambda$ operator in this basis as

$$A = \frac{1}{N_\lambda} \text{Tr}[A] \mathbb{1}_{N_\lambda} + \frac{1}{2} \text{Tr}[A \lambda_i] \lambda_i. \quad (\text{A1})$$

Using the above results, we may identify the coefficients in the second-order cumulant equations [Eq. (5)] as follows:

$$\begin{aligned} \phi_i &= \frac{2i}{N_c} f_{ipr} \sum_\mu \gamma_p^\mu \gamma_r^{\mu*}, \\ \beta_{ij} &= \frac{1}{2} B_p (f_{ipj} - if_{jpi}), \end{aligned}$$

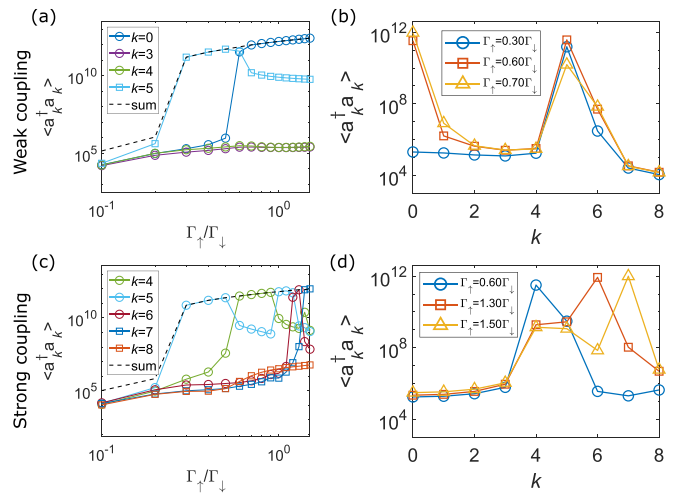


FIG. 13. Time-integrated results with continuous excitation for weak and strong coupling. (a), (c) Pump dependence curves and (b), (d) occupations at different k modes. The mode occupations in (b) and (d) are shown for selected pump powers. The weak-coupling case ($\Omega_R = 0.1$ eV) is shown on the top row and the strong-coupling case ($\Omega_R = 0.4$ eV) on the bottom row.

$$X_{ij} = \xi_{i_k j_k} + i\xi_{i_y j_y},$$

$$\xi_{ij} = 2f_{ipj}A_p + i(f_{ips}\zeta_{rsj} + f_{ris}\zeta_{spj}) \sum_{\mu} \gamma_p^{\mu} \gamma_r^{\mu*}.$$

APPENDIX B: TIME-INTEGRATED THRESHOLD CURVES

In this Appendix we present threshold curves and population distributions obtained by time integrating the photon

mode populations until steady state has been reached. The results shown in Fig. 13 represent a common case in experimental measurements of a system with fast dynamics, where, instead of having access to the temporal evolution of the photon populations, mode populations are collected by integrating over a finite time. Our results show that observing multiple peaks in the time-integrated mode populations can refer to temporal switching between modes.

- [1] L. Furfaro, F. Pedaci, M. Giudici, X. Hachair, J. Tredicce, and S. Balle, Mode-switching in semiconductor lasers, *IEEE J. Quantum Electron.* **40**, 1365 (2004).
- [2] F. Pedaci, M. Giudici, J. Tredicce, and G. Giacomelli, Experimental analysis of mode-hopping in bulk semiconductor lasers, *Appl. Phys. B* **81**, 993 (2005).
- [3] K. A. Shore and D. M. Kane, *Unlocking Dynamical Diversity: Optical Feedback Effects on Semiconductor Lasers* (Wiley, Chichester, 2005).
- [4] A. Gordon, C. Y. Wang, L. Diehl, F. X. Kärtner, A. Belyanin, D. Bour, S. Corzine, G. Höfler, H. C. Liu, H. Schneider, T. Maier, M. Troccoli, J. Faist, and F. Capasso, Multimode regimes in quantum cascade lasers: From coherent instabilities to spatial hole burning, *Phys. Rev. A* **77**, 053804 (2008).
- [5] L. G. Wright, D. N. Christodoulides, and F. W. Wise, Spatiotemporal mode-locking in multimode fiber lasers, *Science* **358**, 94 (2017).
- [6] P. Herre and U. Barabas, Mode switching of Fabry-Perot laser diodes, *IEEE J. Quantum Electron.* **25**, 1794 (1989).
- [7] D. Lenstra and M. Yousefi, Rate-equation model for multi-mode semiconductor lasers with spatial hole burning, *Opt. Express* **22**, 8143 (2014).
- [8] A. Valle, J. Sarma, and K. A. Shore, Dynamics of transverse mode competition in vertical cavity surface emitting laser diodes, *Opt. Commun.* **115**, 297 (1995).
- [9] S. Law and G. Agrawal, Effects of spatial hole burning on gain switching in vertical-cavity surface-emitting lasers, *IEEE J. Quantum Electron.* **33**, 462 (1997).
- [10] A. M. Yacomotti, L. Furfaro, X. Hachair, F. Pedaci, M. Giudici, J. Tredicce, J. Javaloyes, S. Balle, E. A. Viktorov, and P. Mandel, Dynamics of multimode semiconductor lasers, *Phys. Rev. A* **69**, 053816 (2004).
- [11] H. Deng, H. Haug, and Y. Yamamoto, Exciton-polariton Bose-Einstein condensation, *Rev. Mod. Phys.* **82**, 1489 (2010).
- [12] J. Keeling and N. G. Berloff, Exciton-polariton condensation, *Contemp. Phys.* **52**, 131 (2011).
- [13] J. Keeling and S. Kéna-Cohen, Bose-Einstein Condensation of Exciton-Polaritons in Organic Microcavities, *Annu. Rev. Phys. Chem.* **71**, 435 (2020).
- [14] Y. Sun, Y. Yoon, S. Khan, L. Ge, M. Steger, L. N. Pfeiffer, K. West, H. E. Türeci, D. W. Snoke, and K. A. Nelson, Stable switching among high-order modes in polariton condensates, *Phys. Rev. B* **97**, 045303 (2018).
- [15] K. Kusudo, N. Y. Kim, A. Löffler, S. Höfling, A. Forchel, and Y. Yamamoto, Stochastic formation of polariton condensates in two degenerate orbital states, *Phys. Rev. B* **87**, 214503 (2013).
- [16] S. Kim, B. Zhang, Z. Wang, J. Fischer, S. Brodbeck, M. Kamp, C. Schneider, S. Höfling, and H. Deng, Coherent Polariton Laser, *Phys. Rev. X* **6**, 011026 (2016).
- [17] M. Maragkou, A. J. D. Grundy, E. Wertz, A. Lemaître, I. Sagnes, P. Senellart, J. Bloch, and P. G. Lagoudakis, Spontaneous nonground state polariton condensation in pillar microcavities, *Phys. Rev. B* **81**, 081307(R) (2010).
- [18] K. Sawicki, T. J. Sturges, M. Ncieszek, T. Kazimierczuk, K. Sobczak, A. Golnik, W. Pacuski, and J. Suffczyński, Polariton lasing and energy-degenerate parametric scattering in non-resonantly driven coupled planar microcavities, *Nanophotonics* **10**, 2421 (2021).
- [19] T. D. Doan, H. T. Cao, D. B. Tran Thoi, H. Haug, D. Thoi, and H. Haug, Condensation kinetics of microcavity polaritons with scattering by phonons and polaritons, *Phys. Rev. B* **72**, 085301 (2005).
- [20] T. D. Doan, H. T. Cao, D. B. Tran Thoi, and H. Haug, Microcavity polariton kinetics for bosonic condensation and lasing in II-VI compound materials, *Phys. Rev. B* **74**, 115316 (2006).
- [21] C. W. Lai, N. Y. Kim, S. Utsunomiya, G. Roumpos, H. Deng, M. D. Fraser, T. Byrnes, P. Recher, N. Kumada, T. Fujisawa, and Y. Yamamoto, Coherent zero-state and π -state in an exciton-polariton condensate array, *Nature (London)* **450**, 529 (2007).
- [22] N. Y. Kim, K. Kusudo, C. Wu, N. Masumoto, A. Löffler, S. Höfling, N. Kumada, L. Worschech, A. Forchel, and Y. Yamamoto, Dynamical d-wave condensation of exciton-polaritons in a two-dimensional square-lattice potential, *Nat. Phys.* **7**, 681 (2011).
- [23] T. Jacqmin, I. Carusotto, I. Sagnes, M. Abbarchi, D. D. Solnyshkov, G. Malpuech, E. Galopin, A. Lemaître, J. Bloch, and A. Amo, Direct Observation of Dirac Cones and a Flatband in a Honeycomb Lattice for Polaritons, *Phys. Rev. Lett.* **112**, 116402 (2014).
- [24] A. Amo and J. Bloch, Exciton-polaritons in lattices: A nonlinear photonic simulator, *C. R. Phys.* **17**, 934 (2016).
- [25] F. Scafrimuto, D. Urbonas, M. A. Becker, U. Scherf, R. F. Mahrt, and T. Stöferle, Tunable exciton-polariton condensation in a two-dimensional Lieb lattice at room temperature, *Commun. Phys.* **4**, 39 (2021).
- [26] T. Boulier, M. J. Jacquet, A. Maître, G. Lerario, F. Claude, S. Pigeon, Q. Glorieux, A. Amo, J. Bloch, A. Bramati, and E. Giacobino, Microcavity Polaritons for Quantum Simulation, *Adv. Quantum Technol.* **3**, 2000052 (2020).
- [27] P. R. Eastham, Mode locking and mode competition in a nonequilibrium solid-state condensate, *Phys. Rev. B* **78**, 035319 (2008).
- [28] M. Wouters, Synchronized and desynchronized phases of coupled nonequilibrium exciton-polariton condensates, *Phys. Rev. B* **77**, 121302(R) (2008).
- [29] O. Jamadi, F. Réveret, D. Solnyshkov, P. Disseix, J. Leymarie, L. Mallet-Dida, C. Brimont, T. Guillet, X. Lafosse, S. Bouchoule, F. Semond, M. Leroux, J. Zuniga-Perez, and G.

- Malpuech, Competition between horizontal and vertical polariton lasing in planar microcavities, *Phys. Rev. B* **99**, 085304 (2019).
- [30] J. D. Töpfer, H. Sigurdsson, S. Alyatkin, and P. G. Lagoudakis, Lotka-Volterra population dynamics in coherent and tunable oscillators of trapped polariton condensates, *Phys. Rev. B* **102**, 195428 (2020).
- [31] M. Vlaho and A. Eckardt, Nonequilibrium mode competition in a pumped dye-filled cavity, *Phys. Rev. A* **104**, 063709 (2021).
- [32] M. Vlaho, H. A. M. Leymann, D. Vorberg, and A. Eckardt, Controlled two-mode emission from the interplay of driving and thermalization in a dye-filled photonic cavity, *Phys. Rev. Res.* **1**, 033191 (2019).
- [33] J. Marelic, L. F. Zajiczek, H. J. Hesten, K. H. Leung, E. Y. X. Ong, F. Mintert, and R. A. Nyman, Spatiotemporal coherence of non-equilibrium multimode photon condensates, *New J. Phys.* **18**, 103012 (2016).
- [34] C. Kurtscheid, D. Dung, E. Busley, F. Vewinger, A. Rosch, and M. Weitz, Thermally condensing photons into a coherently split state of light, *Science* **366**, 894 (2019).
- [35] A. I. Väkeväinen, A. J. Moilanen, M. Nečada, T. K. Hakala, K. S. Daskalakis, and P. Törmä, Sub-picosecond thermalization dynamics in condensation of strongly coupled lattice plasmons, *Nat. Commun.* **11**, 3139 (2020).
- [36] K. B. Arnardottir, A. J. Moilanen, A. Strashko, P. Törmä, and J. Keeling, Multimode Organic Polariton Lasing, *Phys. Rev. Lett.* **125**, 233603 (2020).
- [37] A. E. Siegman, *Lasers* (University Science Books, Sausalito, CA, 1986).
- [38] J. A. Ćwik, S. Reja, P. B. Littlewood, and J. Keeling, Polariton condensation with saturable molecules dressed by vibrational modes, *Europhys. Lett.* **105**, 47009 (2014).
- [39] A. Strashko, P. Kirton, and J. Keeling, Organic Polariton Lasing and the Weak to Strong Coupling Crossover, *Phys. Rev. Lett.* **121**, 193601 (2018).
- [40] M. d. Jong, L. Seijo, A. Meijerink, and F. T. Rabouw, Resolving the ambiguity in the relation between Stokes shift and Huang-Rhys parameter, *Phys. Chem. Chem. Phys.* **17**, 16959 (2015).
- [41] P. Kirton and J. Keeling, Suppressing and Restoring the Dicke Superradiance Transition by Dephasing and Decay, *Phys. Rev. Lett.* **118**, 123602 (2017).
- [42] M. Sánchez-Barquilla, R. E. F. Silva, and J. Feist, Cumulant expansion for the treatment of light-matter interactions in arbitrary material structures, *J. Chem. Phys.* **152**, 034108 (2020).
- [43] C. Gardiner, *Stochastic Methods: A Handbook for the Natural and Social Sciences*, Springer Series in Synergetics (Springer, Berlin, 2009).
- [44] H.-P. Breuer and F. Petruccione, *The Theory of Open Quantum Systems* (Oxford University Press, Oxford, 2002).
- [45] M. O. Scully and M. S. Zubairy, *Quantum Optics* (Cambridge University Press, Cambridge, 1997).
- [46] J. H. Eberly and K. Wódkiewicz, The time-dependent physical spectrum of light*, *J. Opt. Soc. Am.* **67**, 1252 (1977).
- [47] L. Mazza, S. Kéna-Cohen, P. Michetti, and G. C. La Rocca, Microscopic theory of polariton lasing via vibronically assisted scattering, *Phys. Rev. B* **88**, 075321 (2013).
- [48] T. Gao, P. S. Eldridge, T. C. H. Liew, S. I. Tsintzos, G. Stavrinidis, G. Deligeorgis, Z. Hatzopoulos, and P. G. Savvidis, Polariton condensate transistor switch, *Phys. Rev. B* **85**, 235102 (2012).
- [49] A. Amo, T. C. H. Liew, C. Adrados, R. Houdré, E. Giacobino, A. V. Kavokin, and A. Bramati, Exciton-polariton spin switches, *Nat. Photonics* **4**, 361 (2010).
- [50] A. V. Zasedatelev, A. V. Baranikov, D. Urbonas, F. Scaffrimuto, U. Scherf, T. Stöferle, R. F. Mahrt, and P. G. Lagoudakis, A room-temperature organic polariton transistor, *Nat. Photonics* **13**, 378 (2019).
- [51] D. Ballarini, M. D. Giorgi, E. Cancellieri, R. Houdré, E. Giacobino, R. Cingolani, A. Bramati, G. Gigli, and D. Sanvitto, All-optical polariton transistor, *Nat. Commun.* **4**, 1 (2013).
- [52] A. J. Moilanen, K. B. Arnardottir, J. Keeling, and P. Törmä, Data underpinning Mode switching dynamics in organic polariton lasing, Dataset, University of St Andrews Research Portal, <https://doi.org/10.17630/f4685935-1c0a-414e-a70cd968146985cc> (2022).
- [53] M. Gell-Mann, Symmetries of Baryons and Mesons, *Phys. Rev.* **125**, 1067 (1962).
- [54] M. Stone and P. Goldbart, *Mathematics for Physics: A Guided Tour for Graduate Students* (Cambridge University Press, Cambridge, 2009).